Computers and Geotechnics 148 (2022) 104801

Contents lists available at ScienceDirect

Computers and Geotechnics

journal homepage: www.elsevier.com/locate/compgeo

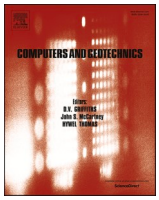

# Influence of slip and permeability of bedding interface on hydraulic fracturing: A numerical study using combined finite-discrete element method

Shan Wu [a,b], Ke Gao [a,b,*], Yu Feng [c,*], Xiaolin Huang [d]

[a] Department of Earth and Space Sciences, Southern University of Science and Technology, Shenzhen 518055, Guangdong, China
[b] Guangdong Provincial Key Laboratory of Geophysical High-resolution Imaging Technology, Southern University of Science and Technology, Shenzhen 518055, China
[c] Institute of Risk Analysis, Prediction and Management (Risks-X), Academy for Advanced Interdisciplinary Studies, Southern University of Science and Technology, Shenzhen 518055, Guangdong, China
[d] Key Laboratory of Shale Gas and Geoengineering, Institute of Geology and Geophysics, Chinese Academy of Sciences, Beijing 100029, China

ARTICLE INFO

*Keywords:*
FDEM
Bedding interface
Hydraulic fracturing
Stress shadow
Fracture interference

ABSTRACT

Shale is a common layered sedimentary rock containing bedding interfaces in oil and gas reservoirs. In hydraulic fracturing of shales, the fracturing fluid could flow into bedding interfaces and cause slipping, thus affecting the propagation of hydraulic fractures. Currently, the interaction mechanism between hydraulic fractures and bedding interfaces is still unclear because of the difficulty in monitoring fractures in laboratory experiments and the lack of appropriate numerical tools to model the dynamic hydraulic fracturing process. In this paper, the emerging combined finite-discrete element method (FDEM) is used to numerically study the main controlling factors of the interaction between hydraulic fractures and bedding interfaces, as it is known for its advantage of simulating material transition from intact solid to crack initiation and propagation. Our results show that the slip property of bedding interfaces determines whether hydraulic fractures can cross over bedding interfaces. Interestingly, the high permeability of bedding interfaces does not hinder the crossing but only delays the time needed for such crossing. We also find that both the slip type and permeability of bedding interfaces can give rise to a change in the width of hydraulic fractures when propagating across bedding interfaces, and result in a discontinuous distribution of local stress and fluid pressure near bedding interfaces accompanied by a strong stress shadow area. Therefore, in the process of hydraulic fracturing in reservoirs with bedding interfaces, the problem of multi-fracture interference could be more deteriorative. This paper aims to provide a new understanding of the hydraulic fracture crossing mechanism and hydraulic fracture morphology in reservoirs with bedding interfaces.

## 1. Introduction

Hydraulic fracturing is a key engineering technique for stimulating oil and gas production in shale reservoirs (Ciezobka et al., 2018; Gandossi, 2013). In hydraulic fracturing, high-pressure fluid is injected into reservoir rocks to form fractures and create flowing channels for oil and gas (Lecampion et al., 2018; Liu et al., 2018). However, shale reservoirs often contain a variety of layered structures such as lithologic patterns, complex laminae, and bedding interfaces (Abbas et al., 2018; Hudson, 2017; Li et al., 2018b; Wu et al., 2019; Zhang et al., 2021a). These layered structures can hinder hydraulic fractures from propagating across beddings and cause a strong multi-fracture interference on the horizontal plane, hence severely limiting the performance of hydraulic fracturing in reservoirs. Therefore, it is vital to investigate the hydraulic fracture propagation mechanism under the influence of bedding interfaces (Cai et al., 2020; Tang et al., 2018; Zhang et al., 2021b).

Existing studies mainly focus on the influence of rock's mechanical properties on hydraulic fracturing, and the important interaction mechanism between hydraulic fractures and bedding interfaces has not yet been fully explored. The few experimental studies in the literature revealed several possible interaction modes between hydraulic fractures and bedding interfaces: (i) hydraulic fractures terminate at bedding interfaces with or without opening of bedding interfaces, (ii) hydraulic fractures propagate straight through bedding interfaces, and (iii)

* Corresponding authors.
*E-mail addresses:* gaok@sustech.edu.cn (K. Gao), fengy3@sustech.edu.cn (Y. Feng).

https://doi.org/10.1016/j.compgeo.2022.104801
Received 12 January 2022; Received in revised form 30 March 2022; Accepted 26 April 2022

hydraulic fractures grow along with bedding interfaces for a certain offset distance before crossing them (Li et al., 2018b; Tan et al., 2017; Zou et al., 2017). Because of the larger permeability of bedding interfaces compared with rock matrix, the injected fluid could easily enter bedding interfaces and thus leads to a fluctuation of fluid pressure in hydraulic fractures (Tang et al., 2018). In addition, the induced stress from hydraulic fractures can cause slipping along bedding interfaces, which results in an increase of fracture width and a redistribution of stress around the tips of hydraulic fractures (Tan et al., 2021). Although these previous laboratory studies qualitatively revealed the influence of permeability and slip of bedding interfaces (Li et al., 2018a; Li et al., 2018b; Tan et al., 2017; Tan et al., 2021; Zou et al., 2017), they lack a quantitative and detailed investigation of how these two factors affect hydraulic fracture propagation. This is mainly because it is challenging to control the properties of bedding interfaces and monitor the hydraulic fracture propagation procedure in laboratory experiments. Therefore, analytical or numerical approaches have to be employed to quantitatively conduct such investigation.

A few attempts have been made to analytically examine how the slip and permeability of bedding interfaces affect hydraulic fracturing. For example, Xu et al. (2019) used an idealized plane strain model to demonstrate that the slip along bedding interfaces can hinder hydraulic fracture propagation, yet they failed to consider the effect of permeability of bedding interfaces. Additionally, as a common drawback, analytical approaches are often restricted to simplistic cases. For numerical approaches, the discrete element method (DEM), boundary element methods (BEM) and finite element method (FEM) are extensively used in hydraulic fracturing simulation. However, these traditional numerical methods all suffer from limitations for the current problem. Specifically, in DEM, many microscopic parameters used in the simulations are difficult to calibrate and thus may lead to uncertain results (Duan et al., 2020; Zhang and Dontsov, 2018); in BEM, it is difficult to realize complex structures such as bedding interfaces (Dontsov and Peirce, 2015). FEM outweighs the above two in terms of discontinuity simulation, in which mainly two ways are seen to be realized to simulate bedding interfaces. One is to set a band of soft finite elements as the bedding interfaces which have mechanical properties smaller than the matrix. By changing the strength and friction parameters, Tan et al. (2021) realized three scenarios of hydraulic fractures, the T-shaped, the passivation, and the crossing fractures. However, because in such models the soft element layers are still continuum and cannot slip explicitly, the effect of slip along bedding interfaces on hydraulic fracturing cannot be directly reflected. The other is to set cohesive zone elements between adjacent finite elements to simulate hydraulic fractures and bedding interfaces. Based on this, Celleri and Sánchez (Celleri and Sánchez, 2021) investigated the effect of bedding interfaces on the propagation of hydraulic fractures and concluded that the permeability of bedding interfaces can reduce fluid pressure and thus prevent the propagation of hydraulic fractures. However, the slip effect along bedding interfaces was not evaluated. Although traditional numerical approaches provide approximated investigation of bedding interfaces, to the best of our knowledge, there is a lack of reliable numerical experiments that account for the effects of both slip and permeability of bedding interfaces simultaneously on hydraulic fracture propagation.

In this paper, we focus on the simultaneous effect of slip and permeability of bedding interfaces. To overcome the limitations of individual traditional numerical approaches, the combined finite-discrete element method (FDEM), which inherits and combines the advantages of both FEM and DEM, is employed to comprehensively study the effect of both slip and permeability of bedding interfaces on hydraulic fracturing (Fu et al., 2011; Lisjak et al., 2017; Munjiza et al., 2020; Yan et al., 2018). FDEM can explicitly simulate the dynamic propagation of hydraulic fractures as well as the slips along fractures and is thus more versatile than pure FEM or DEM. However, challenges still exist in using FDEM to model hydraulic fracturing in layered reservoir rocks with bedding interfaces. The first one lies in the validation of FDEM models. Generally, analytical solutions of hydraulic fracturing are used to verify the results of numerical simulation. Wu et al. (2021) validated the numerical results of FDEM with the analytical solutions of hydraulic fractures in both the toughness and viscosity domains. However, they did not give a clear corresponding relationship between the input parameters used in FDEM and those in the analytical solutions. There are at least two parameters (i.e., tensile strength and fracture energy) for the crack model in FDEM as the input parameter, but there is only one parameter (i.e., fracture toughness) in the analytical solutions. Previous works usually only try to connect the fracture energy with fracture toughness, without considering the tensile strength. Therefore, the correctness of these FDEM simulations of hydraulic fractures cannot be validated completely under a strict restriction of the input conditions. Chen et al. (2009) were aware of the above problem and discussed the different parameters in the crack model that influence the simulation of hydraulic fracturing, but they also did not explain the relationship between the parameters in the crack model and the fracture toughness in the analytical solution. Additionally, in the above FDEM simulations fractures are only allowed to propagate along element boundaries (Ju et al., 2021; Knight et al., 2020; Lisjak et al., 2017; Profit et al., 2016b; Wang et al., 2021b; Zhao et al., 2014); to ensure fracturing simulation accuracy, fine mesh has to be used throughout the model and thus may lower the computation efficiency.

Here, we extend FDEM for hydraulic fracturing simulation with a local adaptive mesh algorithm to not only alleviate the mesh dependency of fracture propagation but also increase the simulation accuracy and computation efficiency. The relationship between the fracture toughness and the parameters in the crack model of FDEM is analyzed, and the numerical results of hydraulic fracture are carefully validated with analytical solutions. We then set up a series of hydraulic fracturing models with bedding interfaces to study the propagation mechanism of hydraulic fractures under the influence of bedding interfaces. The paper is organized as follows. First, we give a brief introduction to FDEM in terms of fracture propagation simulation. Then, we deduce the relationship between the parameters in the crack model and the linear elastic fracture mechanics (LEFM) and set up the numerical models. In Section 3, we present the morphology of hydraulic fracture, injection pressure, and the pressure along the bedding interfaces. In addition, we consider the fracture height, fracture width, and the pressure along the bedding interfaces under different slip scenarios and permeability of bedding interfaces to examine the factors that determine the crossing behavior of hydraulic fractures. In Section 4, we discuss the influence of multi-fractures interference problems in reservoirs with bedding interfaces and give suggestions regarding how the problem may be alleviated in practice. The conclusions are drawn at the end.

## 2. Model

### 2.1. FDEM in a nutshell

The FDEM was originally developed by Munjiza in the early 1990 s to simulate the material transition from continuum to discontinuum (Munjiza, 1992). The essence of FDEM is to merge the algorithmic advantages of DEM with those of the FEM. In FDEM, a discrete fracture is explicitly inserted when a certain fracturing criterion is reached and thus could realize the dynamic transition of material from intact solid to the initiation and propagation of fractures (Lei et al., 2021; Munjiza et al., 2020). Currently, there are several realizations of FDEM, such as the HOSS from the Los Alamos National Laboratory, Y-GEO from the University of Toronto, Solidity from the Imperial College London, and commercial software package IRAZU from the Geomechanica and ELFEN from the Rockfield (Knight et al., 2020; Mahabadi et al., 2016; Profit et al., 2016b; Zhao et al., 2014). We are not intended to give a thorough review regarding the difference between these FDEM branches, and the interested readers could refer to Mohammadnejad

et al. (2021) for more details. In this paper, we use the FDEM realization in ELFEN to simulate hydraulic fracturing because of its advanced and efficient crack simulation capability. The core contents of FDEM in ELFEN in terms of hydraulic fracturing simulation include the Rankine crack model, re-mesh scheme, contact algorithm, and the hydro-mechanical coupling strategy.

### 2.1.1. Rankine crack model and re-meshing

In FDEM, the initiation and propagation of cracks are realized by the explicit insertion of new cracks based on the Rankine crack model. Since hydraulic fracturing mainly involves tensile fractures induced by the splitting effect of injection fluid, only the Mode I type crack is considered in this paper. The generation of tensile fractures using the Rankine crack model is mainly controlled by two parameters, i.e., the tensile strength $ft$ and the fracture energy $G_f$. Once the material has reached the tensile strength, a crack with a defined characteristic length is inserted in the material, and the opening degree of the crack is determined by the fracture energy and local stress state. In the Rankine crack model, a simple linear relationship is assumed between the opening degree, stress state, and fracture energy, as shown in the schematic diagram in Fig. 1a. In some FDEM applications (Lisjak et al., 2013; Zhao et al., 2014), the opening degree and fracture energy are given a nonlinear relationship based on the heuristic scaling function proposed by Evans and Marathe (Evans and Marathe, 1968). Although the nonlinear relationship can capture the nonlinear change of the crack tip, it is difficult to obtain the parameters of the heuristic scaling function for different materials. In most studies, parameters of the heuristic scaling function are simply given fixed empirical values, yet such treatment ignores the difference between materials and may not achieve a desirable approximation to the crack tip.

Generally, the newly generated hydraulic cracks in FEDM are inserted at the interface of solid elements. Although in some FDEM realizations, cracks can be inserted inside the elements based on the local algorithm, the propagation direction of cracks cannot avoid the interferential of mesh (Wang et al., 2021a). To alleviate such influence, we use a local adaptive mesh algorithm to constantly re-mesh the tip of fractures in our model (Fig. 1b). The area around the crack tip is delineated by a damage factor (Wang et al., 2021b). When the factor reaches 80% of the damage threshold, the re-mesh algorithm is activated around the crack tip. This re-mesh algorithm avoids the sensitivity of fracture propagation to the mesh, which could yield more reliable fracture propagation results in the case of multi-fractures with bedding interfaces where hydraulic fractures may propagate in various directions. Another advantage of the local adaptive re-mesh algorithm is its adaptive meshing ability to implement fine meshing at the crack tip of interest and coarse meshing in other areas, which enable a better leverage between computation accuracy and computation efficiency for current numerical investigation.

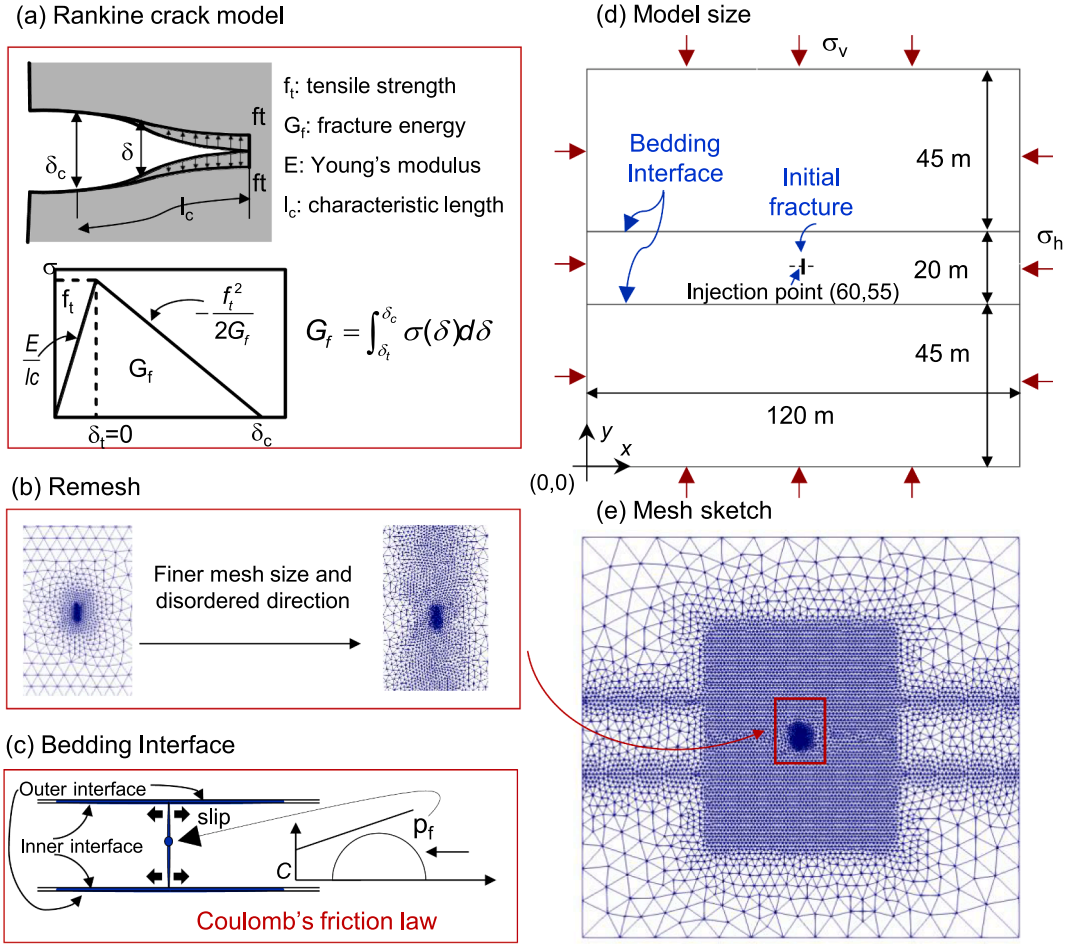


**Fig. 1.** Schematic diagram of the FDEM model for hydraulic fracturing simulation with highly permeable bedding interfaces. (a) The Rankine crack model and the relationship of corresponding parameters. (b) The area around the initial fracture is defined as a re-mesh area, which changes adaptively with the propagation of hydraulic fractures. (c) The bedding interface and its behavior are defined by the Coulomb's law of friction. (d) Sketch of the model. (e) Mesh area of the model. The mesh size of the rock matrix is 10 m; the mesh size at the bedding interfaces and around the well is 1 m; the mesh size around the initial fracture is 0.2 m. The element re-mesh size is also set to 0.2 m.

#### 2.1.2. Contact interaction

When discrete media such as hydraulic fractures and bedding interfaces are inserted into a continuous medium, a contact interaction algorithm is activated in FDEM to process the coupling between the discrete and continuous media. The contact interaction is calculated by using the distributed potential contact force based on the penalty function method. This method could maintain energy balance for discrete elements with various shapes and sizes and yield realistic distributions of contact force (Munjiza and Andrews, 2000; Munjiza et al., 2020). Regarding the contact interaction algorithm, Smoljanović et al. (Smoljanović et al., 2018) proposed an approach that includes modeling of bedding interfaces and fractures by the Coulomb's friction law. In our model, the contact interaction between bedding interfaces can be deemed as a more advanced version, i.e., the one controlled by the Coulomb's friction law plus the plate laminar flow in the problem of hydraulic fracturing.

#### 2.1.3. Hydro-mechanical coupling

The equilibrium of stress and mass conservation provides the governing functions for the problem of hydraulic fracturing in FDEM. The mechanical equation is

$$\boldsymbol{L}^{\mathrm{T}}(\boldsymbol{\sigma}^{e} - \alpha \boldsymbol{m} p_l) + (\rho_l \phi + \rho_s(1-\phi))\boldsymbol{g} = 0, \tag{1}$$

where $\boldsymbol{L}$ is the spatial differential operator; $\boldsymbol{\sigma}^{e}$ is the effective stress tensor; $\alpha$ is the Biot's coefficient; $\boldsymbol{m}$ is a vector$[1 \quad 1 \quad 1]^{\mathrm{T}}$; $p_l$ is the pore pressure; $\rho_l$ is the density of the pore fluid; $\rho_s$ is the density of the solid; $\phi$ is the porosity of the porous medium, and $\mathbf{g}$ denotes the gravity vector.

The seepage equation combining mass conservation along with Darcy's law is

$$\mathrm{div}\left[\frac{k}{\mu_l}(\nabla p_l - \rho_l \boldsymbol{g})\right] = \left(\frac{\phi}{K_l} + \frac{\alpha - \phi}{K_s}\right)\frac{\partial p_l}{\partial t} + \alpha \frac{\partial \varepsilon_v}{\partial t}, \tag{2}$$

where $k$ is the permeability of the porous media; $\mu_l$ is the viscosity of the pore fluid; $t$ denotes time; $K_l$ and $K_s$ are bulk stiffness of the pore liquid and bulk stiffness of the solid, respectively. If the permeability of the reservoir rock (e.g., shale) is extremely low, the $k$, $\phi$ and $\alpha$ are close to zero, resulting in a seepage equation having little influence on hydraulic fracturing. This corresponds to the situation with negligible leak-off of fluid from the fracture.

The flow equation that describes the fluid in the fracture network is

$$\frac{\partial}{\partial x}\left[\frac{k^{fr}}{\mu_l}\left(\frac{\partial p_f}{\partial x} - \rho_f \boldsymbol{g}\right)\right] = S^{fr}\frac{\partial p_f}{\partial t}, \tag{3}$$

and

$$S^{fr} = \frac{1}{e}\left[\left(\frac{1}{K_n^{fr}}\right) + \left(\frac{e}{K_f^{fr}}\right)\right], \tag{4}$$

where $k^{fr} = e^2/12$ is the intrinsic or absolute permeability of the fractured region; $e$ is the aperture of fracture; $\mu$ is the viscosity of the fracturing fluid; $p_f$ is the fluid pressure; $\rho_l$ is the density of fluid; $S^{ft}$ is the storage coefficient of the fracture and is an aperture-based parameter; $K_n^{fr}$ is the normal stiffness of the fracture; $K_f^{fr}$ is the bulk stiffness of the fracturing fluid.

The hydro-mechanical coupling is realized in two steps. First, the pressure within a fracture is calculated based on the flow equation and is transmitted as a pressure boundary for solid elements. Then, the deformation of solid elements is determined based on the mechanical equation and is used as the new fracture morphology to update the pressure within the fractures. Two types of solution algorithms are used in the hydro-mechanical coupling scheme. For the mechanical field, the explicit solution method is used. This approach is efficient to solve problems such as fracturing of materials in which the convergence condition is difficult to achieve. The implicit solution method is used for the fluid field, in which convergence conditions are generally easily enforced. The implicit approach allows for the use of large time increments, thus improving computational efficiency. As the timestep of the implicit solution could be much longer than that of the explicit solution, it is necessary to select an appropriate timestep to transfer the coupling parameters. We use a time factor to control the transfer process of coupling parameters, which is defined as the ratio of timestep for the explicit solution and that for the implicit solution. The larger the time factor is, the higher the coupling error between the fluid and mechanical field would be. Yet, an overly small time factor can lead to a highly expensive computational task. Therefore, it is necessary to optimize the time factor to achieve reasonable computation time and coupling error. In this paper, we chose a time factor of 10, and we will demonstrate later in Section 3 that compared with a smaller time factor of 1, the results show an insignificant difference, but the computation efficiency is substantially enhanced.

### 2.2. Validation

#### 2.2.1. Parametric analysis

We simulate a series of 2D hydraulic fracturing models using the plane strain setup in FDEM. For analytical solutions, the plane strain hydraulic fracture problem was first proposed by Khristianovic and Zheltov (Khristianovic and Zheltov, 1955), i.e., the so-called KGD model. Dontsov (Dontsov, 2017) gave an approximate solution for the KGD model based on the assumption that the global fracture solution is mainly determined by the near-tip behavior and the global fluid volume balance. The KGD solution is usually used for validations of numerical simulations. The solution takes into consideration of fracture toughness ($K_{IC}$), fluid viscosity and leak-off. Two scaling parameters are used for limiting the regimes of the solution, i.e.,

$$K_m = \left(\frac{K'^4}{\mu' E'^3 Q_0}\right)^{1/4}, \tau = \frac{E' C^6}{\mu' Q_0^3} t \tag{5}$$

and

$$E' = \frac{E}{1-\nu^2}, K' = 4\left(\frac{2}{\pi}\right)^{1/2} K_{IC}, \mu' = 12\mu \tag{6}$$

where $K_m$ is the toughness parameter; $E$ is the Young's modulus of rock; $\nu$ is the Poisson's ratio; $K_{IC}$ is fracture toughness; $C$ is the leak-off coefficient of fluid in fracture; $Q_0$ is the injection rate and $t$ is the time of injection.

In Eq. (5), the toughness parameter $K_m$ divides the solution into the viscosity and toughness domain. In the latter domain, the energy of fracture propagation is mainly dissipated in new fracture surfaces. The fracture toughness is the key parameter affecting the results, and fluid viscosity only has a minor effect. In the viscous domain, energy is mainly consumed in the process of fluid flow, while fluid viscosity becomes the dominant parameter, and the effect of fracture toughness can be ignored. The $\tau$ is the dimensionless time that quantifies the influence of leak-off. The leak-off coefficient of fluid in shales is generally small, which is often several orders of magnitude smaller than the injection rate, so it is not considered here for computational efficiency. To validate the proposed FDEM model, we use the KGD solution in the toughness domain for the following calibration.

The property of cracks is defined by the fracture toughness $K_{IC}$, which is based on the theory of linear elastic fracture mechanics (LFEM). The $K_{IC}$ is a parameter that reflects the strength of the material, which includes the influence of initial cracks. So $K_{IC}$ is a parameter for strength, similar to $ft$ in the Rankine crack model. The $K_{IC}$ also has a relationship with the fracture energy $G_{IC}$ based on LFEM. The $G_{IC}$ is similar to $G_f$ in the Rankine crack model. If the Rankine crack model is consistent with the LEFM, the two parameters $ft$ and $G_f$ in the Rankine crack model are

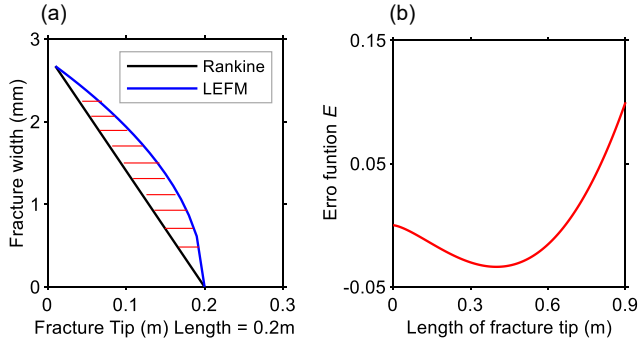


**Fig. 2.** (a) The width of crack tips in the Rankine crack model and LEFM model, respectively; (b) Error function $E$, represents the difference between the two models.

not independent. It is necessary to establish the linkage between $ft$ and $G_f$ to make the Rankine model consistent with LEFM. The relationship between $K_{IC}$ of Mode I crack tip and the opening of the tip of fracture is

$$w(x) = \frac{K'}{E'}(l-x)^{1/2}, \tag{7}$$

where $l$ is the length of the crack tip, and $(l-x)$ is the distance to the crack tip.

For plane strain problems, the relationship between fracture energy $G_{IC}$ and fracture toughness $K_{IC}$ is

$$G_{IC} = \frac{K_{IC}^2}{E}\left(1-\nu^2\right) \tag{8}$$

Combining Eqs. (7) and (8) gives the opening degree of fracture at $x = 0$

$$w(x=0) = \sqrt{\frac{32}{\pi}\frac{G_{IC}}{E'}}l. \tag{9}$$

In the Rankine model, the width at $x = 0$ is equal to

$$\delta_c = \frac{2G_f}{ft}. \tag{10}$$

If the Rankine model satisfies LEFM, the width of the opening should be equal. The characteristic length of the element is the length of the element interface, then$l_c = \sqrt{l^2 + (\delta_c/4)^2}$, as shown in Fig. 1a. Because$\delta_c \ll l$, it can be approximately considered$l_c = l$, and then$l_c = 2(A/\pi)^{1/2}$, where $A$ is the area of the element. Finally, we obtain the relationship between fracture energy $G_f$ and tensile strength $ft$ by combining Eqs. (9) and (10), i.e.,

$$f_t = \sqrt{\frac{G_f \pi E'}{8l_c}}, \tag{11}$$

where $G_f$ is equal to $G_{IC}$ in the Rankine crack model.

The width at the initial position of the crack tip is used to establish the relationship between the Rankine crack model and LEFM based on Eq. (11). However, the changing trend of the width at the fracture tips of the two models is different. The change of the width in the Rankine crack model is linear, and it deviates slightly from LFEM, as shown in Fig. 2a. This results in a smaller crack width as defined by the Rankine crack model than the corresponding crack width defined by $K_{IC}$. The difference between the linear tip and the LEFM tip can be expressed by

$$E = \int_0^l \left[a(l-x)^{1/2} - a\left(-l^{1/2}x + l^{1/2}\right)\right]dx. \tag{12}$$

Let $a = K'/E'$, we have

$$E = a\left(\frac{1}{2}l^{5/2} - \frac{1}{3}l^{3/2}\right). \tag{13}$$

According to this error function $E$, the difference between the two models depends on the length of the crack tip and reaches a minimum when the length is around 0.4 m (Fig. 2b). We thus use a mesh size of 0.2 m in our current numerical model, which guarantees that the error is within an acceptable small range.

The numerical simulation can connect the solution domain of the analytical solution of hydraulic fracturing based on the relationship between the Rankine crack model and LEFM. This makes the results of numerical simulation more reliable. A more outstanding advantage of the Rankine crack model is that it is more suitable to simulate realistic fractures than LEFM when the relationship between the strength and fracture energy of the fracture is nonlinear.

#### 2.2.2. Validation results

The analytical solution of the KGD model in the toughness domain is

$$P_{fracture} = 0.1831\left(\frac{K'^4}{E'Q_0t}\right)^{1/3}, w = 0.6828\left(\frac{K'Q_0t}{E'^2}\right)^{1/3}, l = 0.9324\left(\frac{E'Q_0t}{K'}\right)^{2/3}. \tag{14}$$

According to the relationship between $ft$ and $G_{IC}$ discussed in Eq. (11), we select the parameters in Table 1 for FDEM model validation. The fracture toughness corresponding to the numerical simulation parameters (6.7 MPa) is smaller than that of LFEM (20.6 MPa). The fracture height of the numerical simulation has a very good match with the fracture height in the analytical solution (Fig. 3a). However, the width of the hydraulic fracture in the numerical model is slightly larger than that in the analytical solution at the initial stage because a short crack is prefabricated in the FDEM model to initiate fluid injection (Fig. 3b and d). This also results in a small difference in net pressure with the analytical solution at the initial stage (Fig. 3c). The error of the numerical model is within an acceptable range.

### 2.3. Model setup

#### 2.3.1. Mechanical parameters and meshing

The numerical model for the current analysis is shown in Fig. 1d, which has a dimension of 120 m × 110 m, representing a vertical section in the subsurface with the in-situ stress boundary. The initial fracture is set vertically (in the $y$-direction) in the middle of the model with a length of 0.2 m for perforation. Two bedding interfaces are set horizontally and symmetrically on both sides of the initial fracture. The distance between the two bedding interfaces is 20 m. The length of the bedding interfaces extends throughout to the model boundaries. For the convenience of further reference, we denote the two sides of each bedding interface into

**Table 1**
The parameters for FDEM model validation.

| | | | |
|---|---|---|---|
| Rock Strength, $ft$ | 10.58 MPa | Young's Module, $E$ | 32 GPa |
| Fracture energy, $G_{IC}$ | 1350 N/m | Poison ratio, $\nu$ | 0.2 |
| Characteristic length, $l_c$ | 0.2 $m$ | Injection rate, $Q$ | $1.0 \times 10^{-4}$ $m^3/s$ |
| Theoretical $K_{IC}$ value | 6.7 MPa·$m^{0.5}$ | Viscosity of fracturing fluid, μ | 1 cp |
| $K_{IC}$ for validation | 20.6 MPa·$m^{0.5}$ | Leak-off coefficient, $C$ | $1.0 \times 10^{-12}$ |

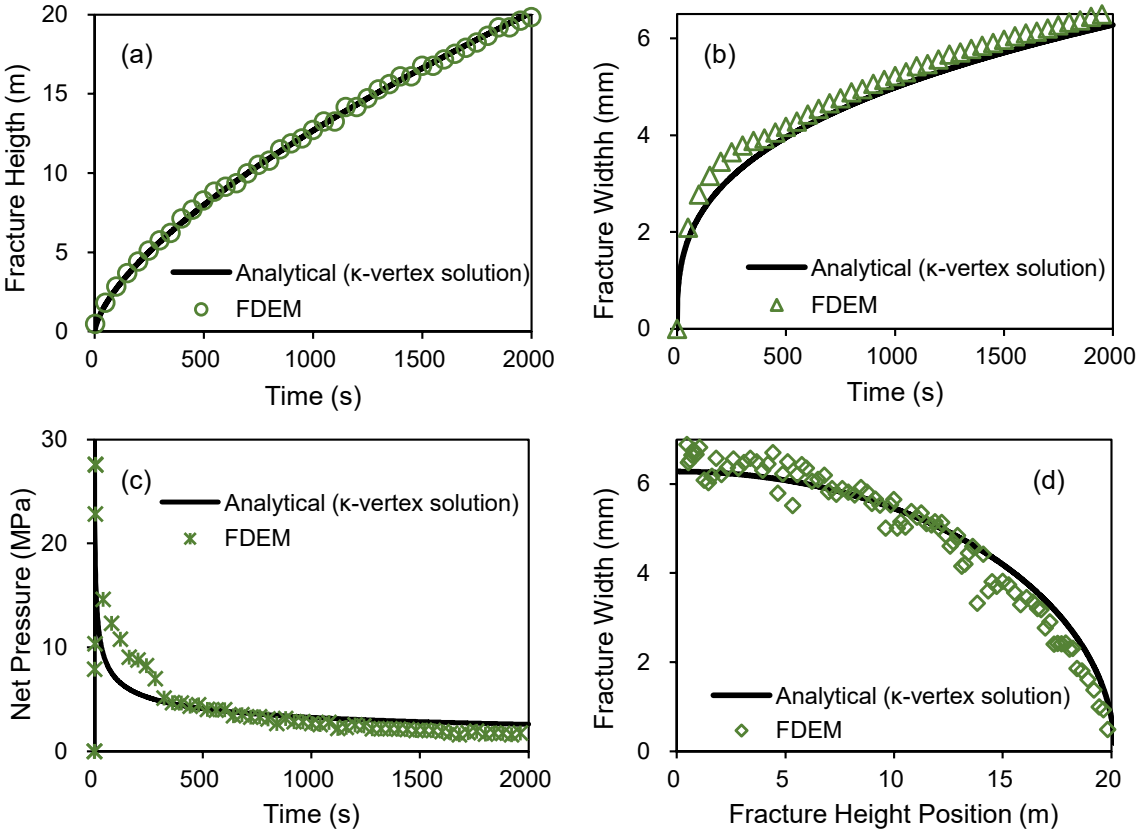


**Fig. 3.** Comparison between the results in FDEM and the analytical solution. (a) The height of fracture; (b) the width of fracture; (c) the net pressure; (d) the changes of fracture width in the direction of fracture height.

an inner sub-bedding interface and an outer sub-bedding interface, according to their relative position with respect to the injection point, as is sketched in Fig. 1c. The contact between the inner and outer sub-bedding interface is controlled by the Coulomb's friction law. The bedding interfaces have higher permeability than the matrix and a plate laminar flow model is used for controlling fluid flow inside bedding interfaces. The main controlling parameter of fluid flow is the hydraulic conductivity, which is related to the permeability of bedding interfaces, i.e.,

$$K = \frac{k\rho_f g}{\mu_f}, \tag{15}$$

where $k$ is the intrinsic permeability of bedding interfaces, which is defined as$k = \frac{e^2}{12}$; $\rho_f$ is the density of the fluid; $\mu_f$ is the fluid viscosity.

A detailed selection of parameter values for the bedding interfaces is given in the following sections. In addition, all the rock matrices in the model have the same properties. We use the parameters in the validation model shown in Table 1 for the following simulation. The modeling domain is discretized in a mesh of unstructured triangular elements of different sizes (Fig. 1e). The mesh size for the rock matrix is 10 m and that in the area around the bedding interfaces is 1 m. A mesh refinement region is set around the initial fracture with a mesh size of 1 m. The mesh size at the initial fracture tips is set to 0.2 m. As the fracture propagates, the local adaptive mesh algorithm will take effect automatically to maintain a fine mesh at a size of 0.2 m around the fracture tip. This mesh size is selected according to the existing literature on the simulation of similar hydraulic fracturing problems, which can guarantee the accuracy of simulation results and also limits the computational cost to an acceptable range (Ju et al., 2019; Lisjak et al., 2017; Yan et al., 2016). By doing this, the mesh dependency problem could be alleviated, and the advantages of such a technique have been demonstrated in published works (Profit et al., 2016a; Profit et al., 2016b) and ELFEN User and Theory Manual (Rockfield, 2016).

### 2.3.2. *Three bedding slip scenarios*

When hydraulic fractures propagate vertically approaching the bedding interfaces, the pressure (in the horizontal direction) in the hydraulic fracture (Fig. 1c) may cause the slip of bedding interfaces under certain conditions. There are three scenarios of slip conditions for the bedding interface. In scenario 1, the bedding interface does not slip, when the pressure in the hydraulic fracture is maintained less than the frictional resistance of bedding interface during the crossing process of hydraulic fracture. In Scenario 2, the slip is induced by the reduction of effective normal pressure on the bedding interface after the hydraulic fluid enters the bedding interface. This essentially occurs due to the decrease of frictional resistance in the bedding interface. In scenario 3, the pressure in the hydraulic fracture is greater than the frictional resistance of the bedding interface in conditions without the rise of fluid pressure in the bedding interface and thus results in a slip of bedding interface before the fracture fluid entering the bedding interface. Frictional resistance of bedding interface could be determined by the friction coefficient and cohesion of bedding interfaces based on the Coulomb's friction law. We adjust the friction coefficient and fix the cohesion to realize the above three slip scenarios.

To select appropriate friction coefficients, the stress state in each slip scenario needs to be defined. The pressure in the vertical hydraulic fracture is determined by

$$P_f = P_{net} + \sigma_{h,} \tag{16}$$

where $P_{net}$ is the net pressure in hydraulic fracture; $\sigma_h$ is the minimum horizontal in-situ stress. According to the Coulomb's friction law, the condition for slip along the bedding interface should satisfy

$$P_f \geqslant 2(\sigma_v - P_{if})\mu + 2C. \quad (17)$$

Substituting Eq. (16) into Eq. (17) gives

$$P_{net} \geqslant 2(\sigma_v - P_{if})\mu + 2C - \sigma_h, \quad (18)$$

where $\sigma_v$ is the vertical in-situ stress, μ is the friction coefficient of the bedding interface, $C$ is the cohesion of bedding interface and $P_{if}$ is the pore pressure in the bedding interface. Before the hydraulic fracturing fluid enters the bedding interface, $P_{if}$ is set to 0 MPa. When the hydraulic fracturing fluid enters the bedding interface, the maximum pore pressure in the bedding interface satisfies$P_{if} = P_f$. Substituting the two $P_{if}$ values into Eq. (17) gives the two critical friction coefficients, i.e.,

$$\mu < \frac{P_{net} + \sigma_h - 2C}{2\sigma_v} = \mu_1, \quad (19)$$

and

$$\mu < \frac{P_{net} + \sigma_h - 2C}{2(\sigma_v - \sigma_h - P_{net})} = \mu_2, \quad (20)$$

where $\mu_2$ is larger than$\mu_1$. In our numerical model, the in-situ stress of $\sigma_v = 30$ MPa and $\sigma_h = 10$ MPa is used as boundary loadings (Fig. 1c) according to the field data. The cohesion is set to 3 MPa, which is within the reasonable range of cohesion for bedding interface in shales. The rock mechanics properties are the same as those used for model validation, so the net pressure $P_{net}$ at the position of bedding interfaces can be obtained from the validation results and is 3.5 MPa. According to Eq. (19) and (20), based on the value of in-situ stress, cohesive and $P_{net}$, we obtain the $\mu_1$ and $\mu_2$ as 0.12 and 0.21, respectively. If the friction coefficient $\mu$ is larger than $\mu_2$ (0.21), the stress state cannot induce the slip along bedding interface (Scenario 1). In Scenario 2, the bedding interface slips due to the increase of fluid pressure in the bedding interfaces, and the friction coefficient $\mu$ should be somewhere between $\mu_1$ (0.12) and $\mu_2$ (0.21). If $\mu$ is smaller than $\mu_1$ (0.12), the slip of bedding interface occurs before the fracture fluid enters the bedding interface (Scenario 3).

#### 2.3.3. Experiment design

To investigate the simultaneous effect of permeability and slip of bedding interface on hydraulic fracturing, we arrange several numerical cases with different permeability and slip scenarios, and all cases are with the same injection parameters and stress state as the ones used for model validation. The permeability of the bedding interface is evaluated based on the statistical aperture size of natural fractures in shales. Generally, the aperture of bedding interface is close to that of natural fractures in a range from 1 μm to 87 mm (Ling et al., 2021; Vega et al., 2015; Wang and Gale, 2016; Zou et al., 2016), which corresponds to a variation of permeability from 0.08 D to 630 D. We use four permeabilities in our model, i.e., 1 D, 10 D, 50 D, and 100 D. Although the selected values of permeability do not cover the whole range of realistic permeability, the results of each case will be discussed in detail in terms of pressure and fracture morphology and thus give sufficient references to other possible permeability values. Three slip scenarios are prepared using three friction coefficients – 0.35 (Scenario 1), 0.18 (Scenario 2) and 0.08 (Scenario 3), according to the discussion in the previous section. We speculate that in the case of Scenario 1 with low permeability, the influence of bedding interface will be nearly negligible, and the hydraulic fractures will propagate similarly to that in intact rocks; while with the increasing permeability and decreasing friction coefficient, the effect of bedding interface on hydraulic fracturing is expected to rise. The parameter design of each numerical case is shown in Fig. 4.

## 3. Results

Our FDEM simulations have been conducted using the commercial ELFEN software (TGR4.0). For each model consisting of 20,898 linear triangle elements, it takes ~ 400 min CPU time on a single core of the Intel Xeon Gold 6230 CPU 2.10 GHz processor. Because of the model setup, the simulated hydraulic fracture mainly propagates in the direction of $\sigma_v$ (y-axis) and opens in direction of $\sigma_h$ (x-axis). Fig. 5 presents the hydraulic fracturing results in two extreme cases, i.e., Scenario 1 with 1 D permeability and Scenario 3 with 100 D permeability, which respectively exhibits the crossing of hydraulic fracture over bedding interface and the non-crossing phenomenon. For the models prepared, we investigate and present the effect of bedding interfaces on the propagation of hydraulic fractures by comparing the models with and without bedding interfaces. The fracture height, slip displacement along bedding interfaces, fracture width, and injection pressure in each case are evaluated. Also, the pressure along the bedding interfaces for each case is analyzed to reveal the change of local stress during the contact between hydraulic fracture and bedding interface.

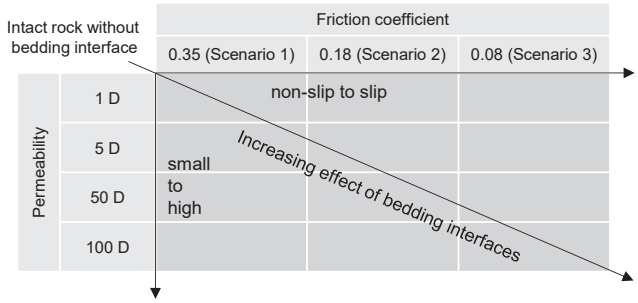


**Fig. 4.** The experiment design for each numerical case.

### 3.1. Influence of bedding interface on fracture height

Here, fracture height is the length of hydraulic fracture in the *y*-direction, i.e., the normal direction of the bedding interface (Fig. 5a). If bedding interface hinders the propagation of hydraulic fracture, the fracture height stops growth; thus the fracture height could reflect the interaction between hydraulic fractures and bedding interfaces (crossing or non-crossing). Due to the symmetry of hydraulic fracture in the *y*-direction, we use the half-length of fracture height to characterize the growth of hydraulic fracture. The half-length of fracture height in each case increases with time, but deviates from each other when meeting the bedding interface, i.e., at 10 m half-length (Fig. 6a). For the four cases in Scenario 3, the hydraulic fractures propagate upwards and terminate at the bedding interfaces (Fig. 6a). While in cases in Scenarios 1 and 2, the growth of the height of hydraulic fractures pauses for a while and then continues to increase after propagating across the bedding interfaces.

For cases in Scenario 3, the slip along bedding interfaces is the dominant cause of the termination of hydraulic fracture at bedding interface. While in the crossing cases, i.e., all the cases in Scenarios 1 and 2, the crossing time is more affected by the permeability of bedding interfaces than the slip mode (Fig. 6b). In the crossing cases with 1 D permeability, the height of hydraulic fracture grows slightly slower than the case without bedding interfaces (black line). While in the crossing cases with higher bedding interface permeability (larger than 1 D), the hydraulic fractures suspend at the bedding interface for nearly 150 s and then continue to propagate and cross over the bedding interface. Finally, the fracture height in all crossing cases with bedding interface almost reaches the same value as that in the case without bedding interface (Fig. 6c). The above results demonstrate that although the permeability of bedding interfaces can impede the growth of fracture height for a certain time, it will not prevent the final growth of hydraulic fractures. Additionally, compared with the case without bedding interface, the hydraulic fractures in the cases with bedding interfaces have an accelerated growth speed after crossing the bedding interfaces, as is

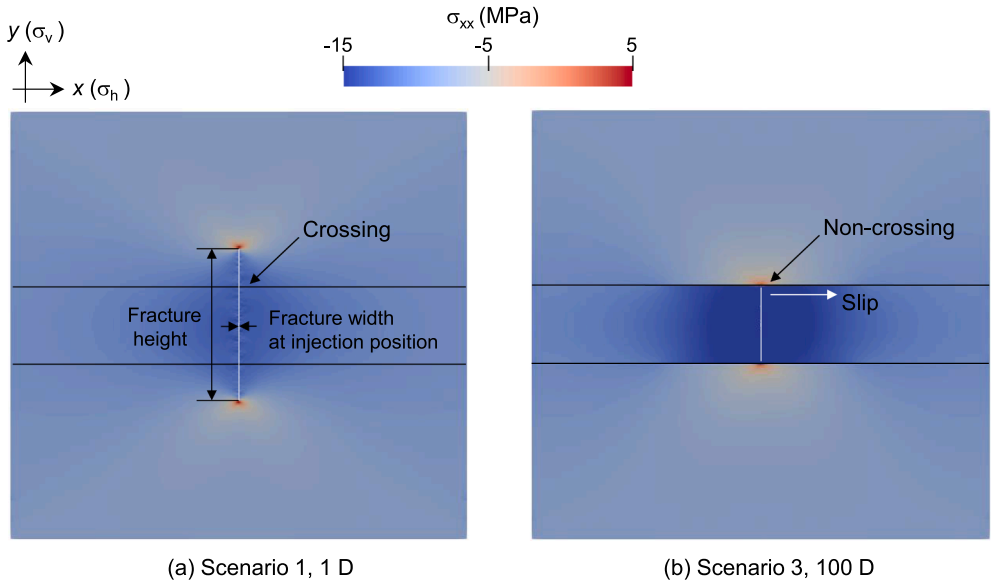


**Fig. 5.** Hydraulic fracturing results in two extreme cases (compressive negative sign convention is used for stress visualization).

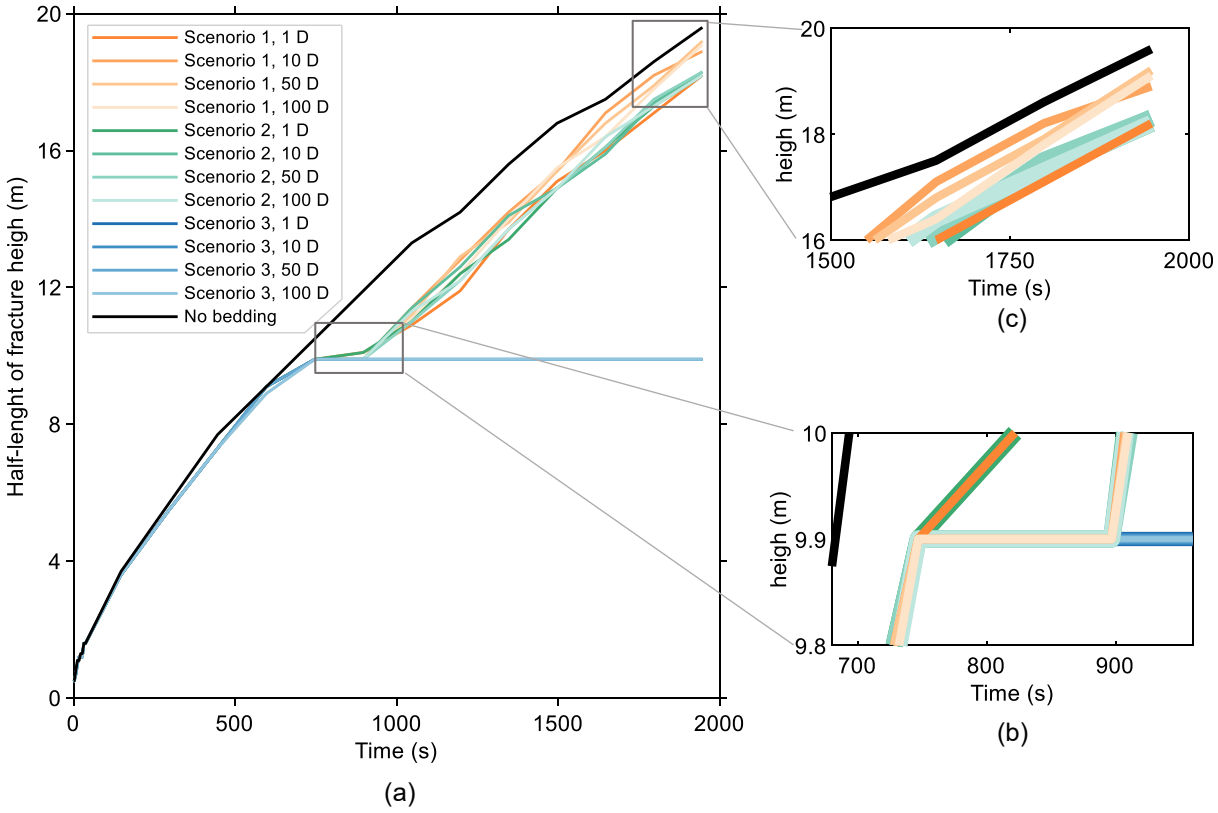


**Fig. 6.** The growth of fracture height versus time. The slip of bedding interface (Scenario 3) stops the growth of hydraulic fractures. The crossing time of hydraulic fractures through the bedding interfaces is controlled by the permeability of bedding interface.

manifested by the relatively larger slopes of fracture height with respect to time (Fig. 6a).

### 3.2. Slip displacement along bedding interface

Fracture morphology can be used for optimizing hydraulic fracturing and has been discussed in many studies related to the propagation of hydraulic fractures (Lecampion et al., 2018; Tang and Wu, 2018; Wu et al., 2019; Xu et al., 2019). The slip displacement along bedding interfaces induces the difference of fracture width at the position between the inner and outer bedding interfaces, thus bringing a discontinuity outline of the fracture morphology. We present detailed changes in fracture morphology in this section. Fig. 7a-c sketch the outlines of fracture morphology represented by the fracture opening over the direction of fracture height beginning from the injection point. We only present the fracture morphology in three scenarios with 1 D bedding interface permeability, because other cases in the corresponding slip scenario show a proximate fracture morphology.

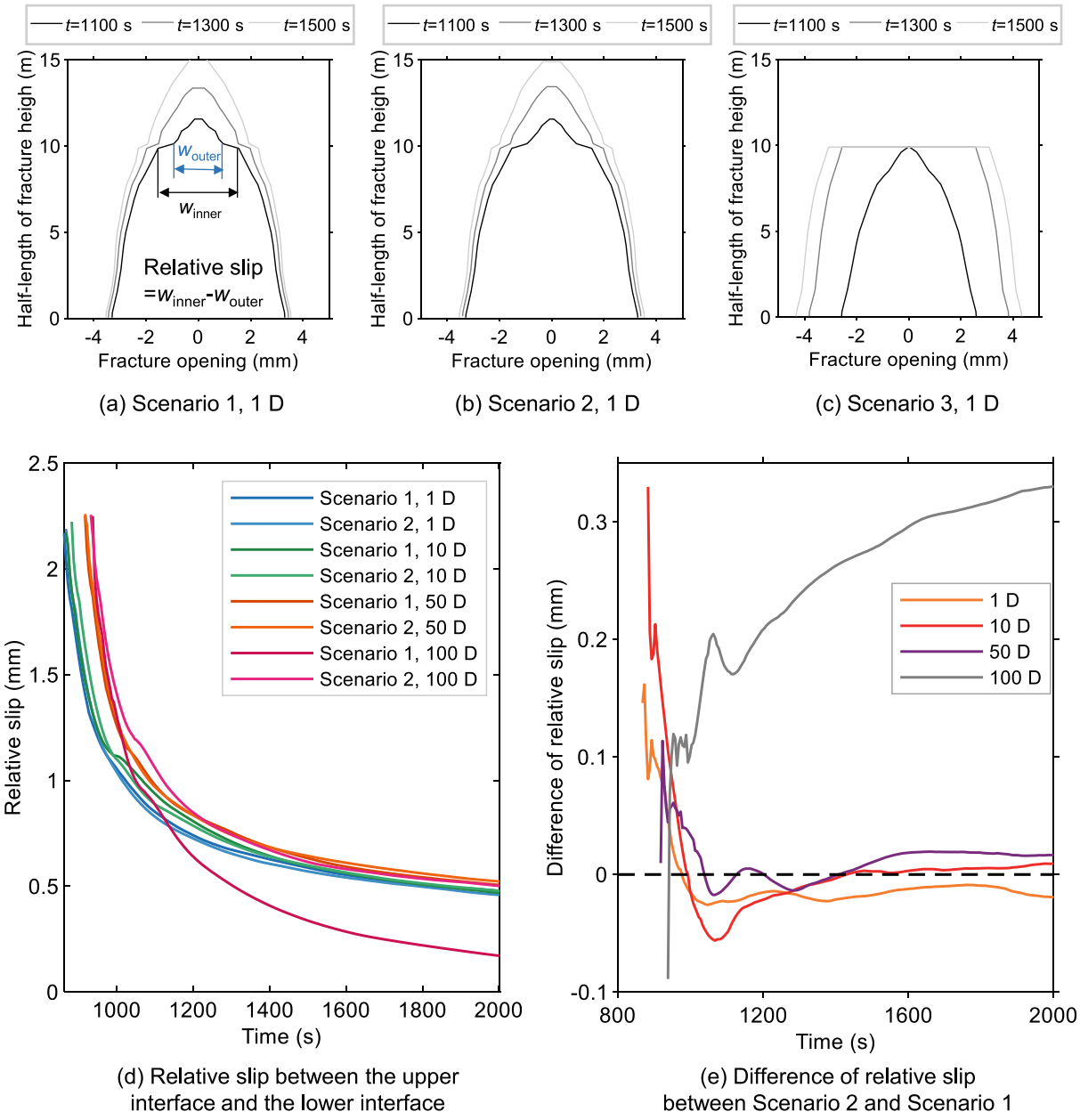


**Fig. 7.** (a)-(c) Hydraulic fracture morphologies under three slip scenarios; (d) the relative slip changes over time; (e) the difference of the relative slip between Scenario 2 and Scenario 1 versus time.

In the crossing cases (Scenarios 1 and 2), the relative slip distance between the inner and outer bedding interface, defined as the difference of fracture opening, reaches its maximum when the hydraulic fracture just crosses the bedding interface (Fig. 7d). Then, the relative slip decreases gradually and reaches a stable value (Fig. 7d), which is similar to a healing process for eliminating relative slip. However, relative slip in the non-crossing cases (Scenario 3) increases gradually over time due to the continuous opening of hydraulic fracture (Fig. 7c), in which such a healing process of relative slip is absent. Among the crossing cases containing a healing process, the relative slip in Scenario 1 with 100 D permeability exhibits a quite different value from that in other cases. We calculate the difference in terms of relative slip between Scenario 1 and Scenario 2 for cases with the same permeability using the relative slip in Scenario 2 minus that in Scenario 1. The difference presented in Fig. 7e reveals that in the case with 1 D permeability the result is negative, which means that the relative slip in Scenario 2 is smaller than that in Scenario 1. The difference is close to 0 in the case with 10 D permeability. The relative slip in Scenario 2 is large than that of Scenario 3 in the case with 50 D and 100 D permeability. Particularly, in the case with 100 D, there is a large difference in the relative slip between Scenario 2 and Scenario 1. Previous studies claimed that the influence of bedding interface on fracture morphology is similar to that of higher fracture toughness on rock, which leads to a wider fracture width and shorter fracture length (Xu et al., 2019). Our numerical results demonstrate a more detailed influence of bedding interface on fracture morphology. In the process of hydraulic fracture propagation, larger relative slips appear at the bedding interface for the lower permeability cases, and the reservoir shows higher "fracture toughness". In contrast, smaller relative slips appear in the high permeability cases, which means the reservoir has an insignificant improvement of "fracture toughness".

### 3.3. Fracture width and pressure at injection point

Fracture width and pressure at the injection point are commonly

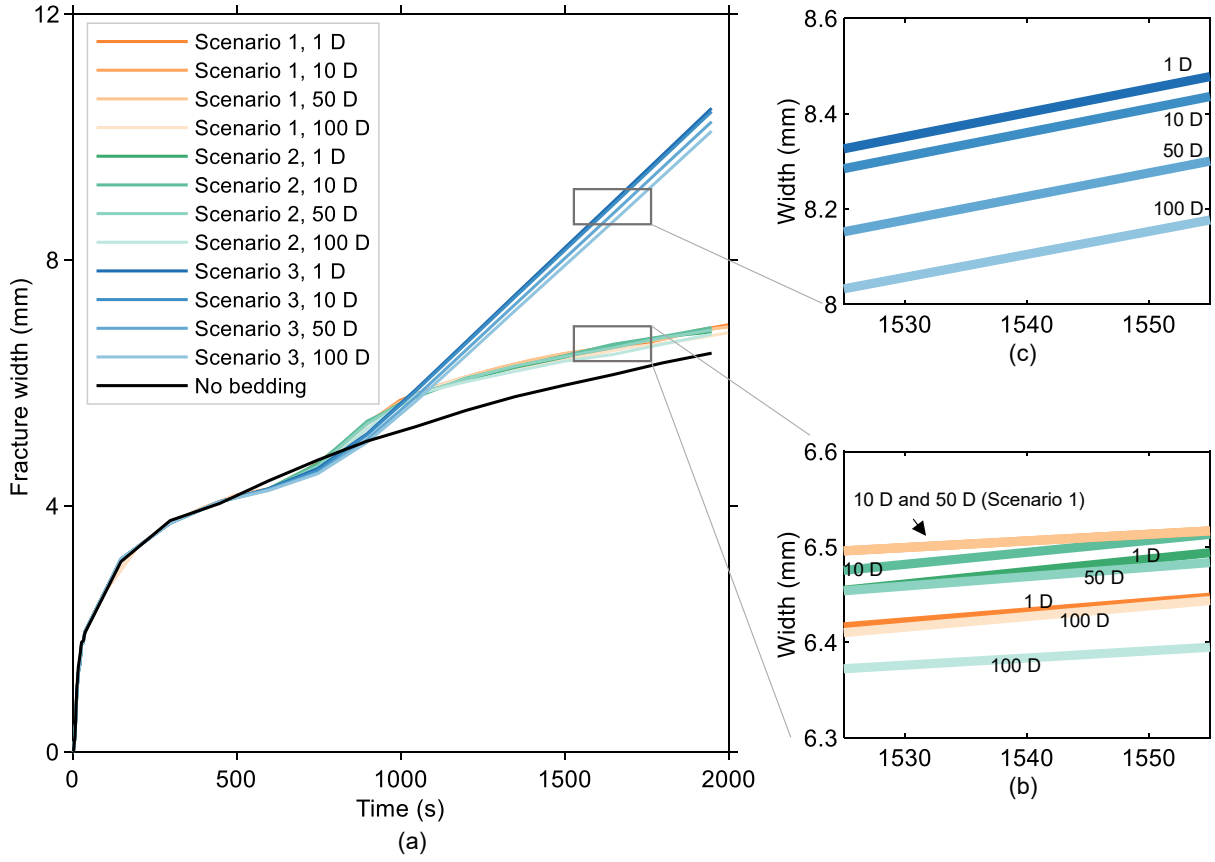


**Fig. 8.** Variation of fracture width with time at the injection point.

monitored to instruct fracturing strategy in the oil and gas field. It is necessary to know whether the influence of bedding interface on hydraulic fracturing can be reflected by the fracture width and pressure at the injection point. Therefore, we extract the fracture width and pressure at the injection point in each case for comparison. It can be seen from Fig. 8 that, in Scenario 3, the fracture width at the injection point increases with the decreasing permeability of bedding interfaces, and for a given permeability the fracture width increases linearly with time after the slipping of bedding interfaces (Fig. 8a). It seems the fracture width could reflect the influence of bedding interface permeability on fracture propagation. However, the fracture width in each case in Scenarios 1 and 2 cannot reveal the difference in the permeability of bedding interfaces (Fig. 8b). For Scenarios 2 and 3, the fracture widths have a complex changing process compared with the case without bedding interface, in that they decrease slightly before hydraulic fracture crossing over the inner interface and then increase after the hydraulic fracture crossing over the outer interface. The reason for the decrease may lie in that when the hydraulic fractures approach the inner interface, the effective fracture toughness in the area near the bedding interface is small due to the weak fracture toughness of bedding interfaces, which results in a smaller fracture width. After hydraulic fracture crosses over the outer interface, the fracture width in the case with bedding interfaces is wider than that in the case without bedding interface; but the former gradually converges to the value of the latter, indicating that the influence of bedding interface on fracture width slowly weakens, which is similar to the gradual decrease of relative slip shown in Fig. 7d.

Fig. 9 presents the pressure profile at the injection point. In Scenario 3, when the bedding interface starts to slip, the pressure increases linearly; the smaller the permeability is, the higher the pressure would be (see inset of Fig. 9). In Scenarios 1 and 2, the pressure decreases slightly until the hydraulic fracture crosses over the bedding interface.

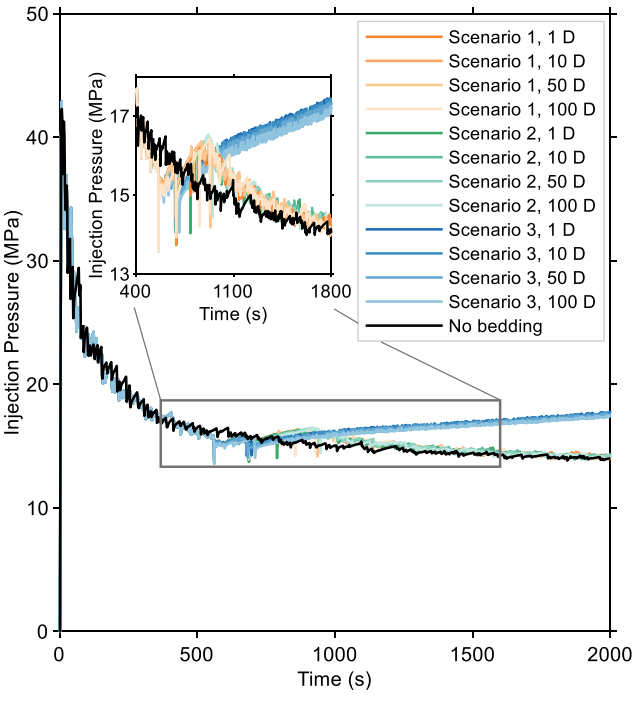


**Fig. 9.** Evolution of pressure at the injection point.

After that, the pressure increases and converges to the pressure in the case without bedding interface. During the crossing process of hydraulic fracture, the duration time of pressure fluctuation is short, and the fluctuation amplitude is small (inset of Fig. 9). The pressure curves in the

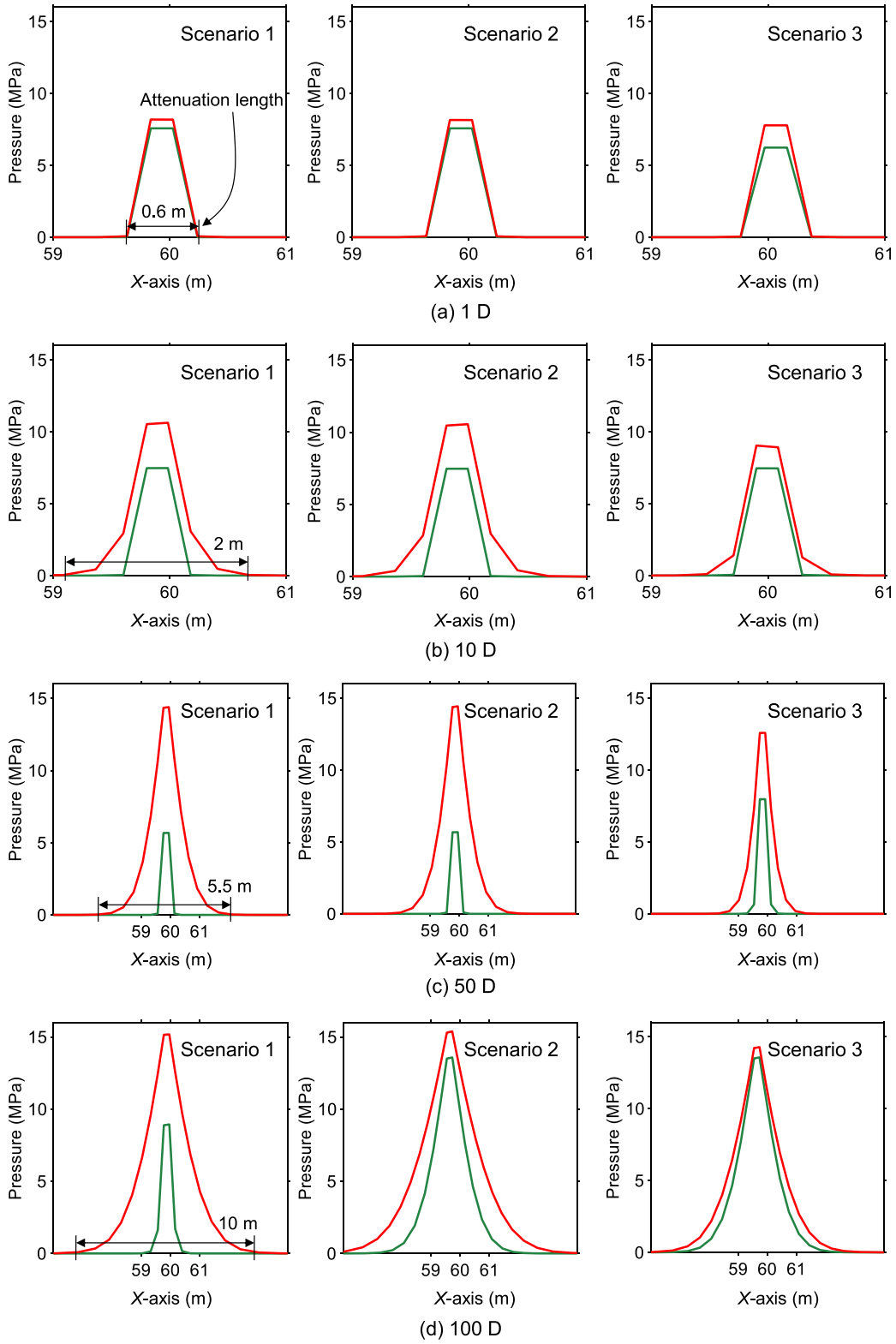


**Fig. 10.** Pressure distribution along bedding interface for models with different slip scenarios and bedding interface permeability. Please note that the location of the injection point is at × = 60 m, so the position of the intersection of the hydraulic fracture and the bedding interface is also roughly at × = 60 m.

cases of Scenario 1, Scenario 2, and in the case without bedding interface, almost coincide.

The change of fracture width and pressure at the injection point can reflect whether the bedding interface slips and hydraulic fractures cross over the bedding interfaces. However, it is difficult to identify how the bedding interfaces affect the propagation of hydraulic fracture, because in Scenarios 1 and 2, the difference of fracture width and pressure at the injection point between the cases with and without bedding interface is small.

### 3.4. Pressure distribution along bedding interface

When hydraulic fluid enters bedding interfaces, an increase of pressure inside bedding interfaces could be observed. The distribution of fluid pressure inside bedding interfaces could reveal how the permeability of bedding interfaces affects hydraulic fracture propagation. We show the pressure along the bedding interfaces in Fig. 10 at the two typical time stamps, i.e., when the hydraulic fracture just crosses over the inner interface (green line), and when the hydraulic fracture just crosses over the outer interface (red line). In Scenarios 1 and 2, the pressure witnesses a clear rise between the two typical time stamps. For Scenario 3, since the hydraulic fracture cannot cross over the outer interface, the red line reaches a stable value when the hydraulic fracture touches the bedding interface, and eventually results in a higher pressure than that in cases where hydraulic fracture can cross over the outer interface. In all cases with lower permeability (e.g., 1 D and 10 D), the peak value of the pressure (at the time when the hydraulic fracture crosses the inner bedding interface, green line) in Scenario 3 is less than that in Scenarios 1 and 2, while such pressures in Scenarios 1 and 2 approximately reach the same value. In all cases with higher permeability (e.g., 50 D and 100 D), the peak pressure (green line) displays the following order for the three scenarios: Scenario 3 > Scenario 1 > Scenario 2. The peak values of the red lines in Scenarios 1 and 2, which represent the pressure when crossing over the outer interface, are higher than the stable pressure in Scenario 3. It is difficult to explain how the permeability of bedding interface affects the pressure because the slip scenario of bedding interface also disturbs the value of pressure. Nevertheless, the distribution of fluid pressure, which is horizontally symmetric with respect to the intersections between the hydraulic fracture and bedding interface, shows a close relationship with the permeability of bedding interfaces. The attenuation of pressure on the bedding interface spans a certain length. From the results shown in Fig. 10, this attenuation length is controlled by the permeability of bedding interfaces: 0.6 m attenuation length corresponds to the permeability of 1 D, 2 m to 10 D, 5.5 m to 50 D, and 10 m to 100 D. The various slip scenarios affect the attenuation length slightly in the cases with the same permeability. The cases in Scenario 3 have the shortest attenuation length, which signifies that the slip of bedding interface inhibits the transmission of pressure on the bedding interface.

The attenuation length of pressure on the bedding interface is limited, which can be explained by the pressure distribution in plate laminar flow. According to the formula of pressure distribution for plate laminar flow

$$Q = -\frac{kA}{\mu}\frac{dP}{dx} \tag{21}$$

(where $Q$ is the fluid rate; $k$ is the permeability; $A$ is the aperture of the plate; μ is the fluid viscosity; $dP/dx$ represents the distribution of pressure along the plate), the attenuation length of pressure is related to the permeability of bedding interface and the pressure at the contact position of bedding interface and hydraulic fracture. The pressure on the contact position is approximately proportional to the net pressure in the hydraulic fracture, and it is large near the injection point and remains at a relatively steady low value far away from the injection point. Therefore, the pressure at the contact position is nearly the same when the contact position is far away from the injection point, which indicates that the permeability of bedding interface mainly controls the attenuation length of pressure on the bedding interface.

If the length of bedding interface is shorter than the attenuation length, fracturing fluid will flow out of the boundary of the model, yielding the possibility for the hydraulic fracture to cross the bedding interface. When the permeability of bedding interface is greater than 1 D, the attenuation length reaches meter level. Since it is easy for the fluid to flow out of the boundary in a meter-scale physical laboratory experiment, it is difficult to observe hydraulic fracture crossing over the bedding interface in rocks with highly permeable bedding interfaces in the laboratory. It should be noted that the reason for the failure of bedding interface crossing lies in the flowing out of fluid in the system, rather than the high bedding interface permeability. Therefore, under reservoir conditions where no boundary exists for fluid to flow out, the high bedding interface permeability is not responsible for the prevention of hydraulic fractures from crossing over the bedding interface.

## 4. Discussions

### 4.1. Stress shadow

Stress shadow is an area in reservoir rocks where the initial in-situ stress state is affected by hydraulic fractures (Nagel et al., 2013; Taghichian et al., 2014). In the process of multi-cluster hydraulic fracturing, stress shadow is the main causing factor of fracture interference (Liu et al., 2020; Yang et al., 2020), which could yield uneven propagations of hydraulic fractures and weaken the effectiveness of hydraulic fracturing. Therefore, it is important to monitor fracture interference during multi-cluster hydraulic fracturing. The fracture interference is usually monitored by observing the pressure at injection point. Our results show that the change of injection pressure is small in the cases when hydraulic fracture could cross over the bedding interface. However, large changes in stress can occur on bedding interface in reservoirs where the stress shadow also changes a lot. To illustrate this, we define a parameter to quantify the effect of stress shadow. Generally, the opening direction of hydraulic fracture follows the direction of minimum in-situ stress, and the stress shadow in this direction is usually larger than that in the fracture propagation direction. Therefore, we define the parameter based on the minimum in-situ stress as

$$R = \frac{\sigma_h + \sigma_{h\_initial}}{\sigma_{h\_initial}}. \tag{22}$$

A higher $R$ value indicates a stronger stress shadow that could lead to more serious fracture interference.

In intact rock, the stress shadow attenuates rapidly in areas far away from hydraulic fractures. The ratio $R$ of stress shadow is less than 0.4 in areas about 30 m away from the fracture in $\sigma_h$ direction (Fig. 11a). For the rock containing bedding interfaces, we use the cases with 1 D permeability under the three slip scenarios to display the stress shadow (Fig. 11b, c and d), because different bedding interface permeability has little influence on stress shadow. In Scenarios 1 and 2, the stress shadow in the middle layer is larger than that in areas outside the bedding interface (Fig. 11b and c). In Scenario 3, the stress shadow increases continuously in the middle layer and spreads away from the hydraulic fracture, resulting in a large area of stress relief outside the bedding interface (Fig. 11d). In essence, the area of stress shadow depends on the width of hydraulic fractures. When the width is large, the hydraulic fracture poses a greater pushing pressure on the surrounding medium and forms the stress shadow. In the case in Scenario 3, the width of hydraulic fracture keeps increasing in the middle layer, causing a large area of stress shadow (Fig. 11d). However, under the conditions of Scenarios 1 and 2, the width of hydraulic fracture over time converges to that of the case without bedding interface. This indicates that the stress shadow caused by bedding interface is comparable to that in the case

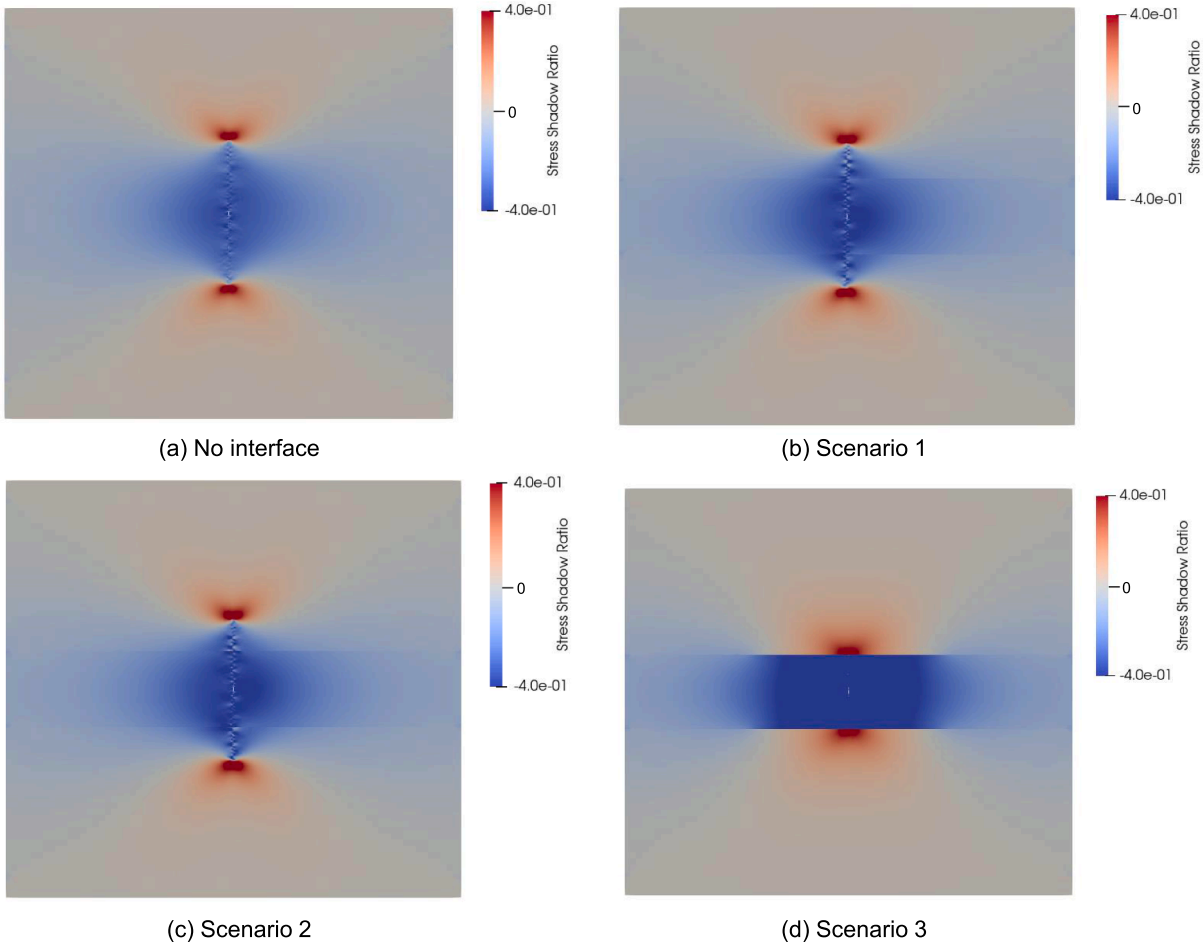


**Fig. 11.** The stress shadow in each case. The permeability of bedding interfaces in (b), (c), and (d) is 1 D.

without bedding interface. Therefore, under the conditions of Scenarios 2 and 3, the influence of stress shadow can be reduced by fracturing a single cluster fracture with sufficient time to eliminate the influence of bedding interfaces on the width of hydraulic fracture. We also need to pay attention to the fracture interference caused by fluid pressure. According to the distribution of fluid pressure on bedding interface (Fig. 10), larger fracture interference may be caused by the fluid pressure on bedding interface when multiple fractures propagate towards the bedding interface altogether. The fluid pressure can interfere between adjacent hydraulic fractures through bedding interfaces if the space between hydraulic fractures is less than the attenuation length of pressure on bedding interface.

### 4.2. Limitations

The slip scenarios of bedding interface in this paper are universal, and it is thus unnecessary to consider the influence by analyzing multiple parameters that control the slip (i.e., cohesive stress and friction coefficient). However, in the process of field hydraulic fracturing, the slip scenario of bedding interface is more complicated, and the three scenarios examined in this paper may occur simultaneously. Two possible reasons for this are as follows. First, the fluid pressure in hydraulic fracture is large near the injection point and gradually reaches a stable value when moving away from the injection point. Therefore, the slip scenario of bedding interface near the injection point is more likely to be Scenario 3, and that in places far away from the injection point may be Scenario 1 or 2. Second, the cohesive stress and friction of the bedding interface are heterogeneous in nature and can also result in a combination of the three scenarios. In our model, the opening of bedding interfaces is kept constant during the slip. The process of slip may affect the opening of bedding interfaces and further affect the parameters such as permeability, cohesion stress, and friction coefficient of bedding interface, resulting in a complex slip scenario. In addition, the distribution of fluid pressure on bedding interface is more complex than that calculated based on the plate laminar flow. In the current model, the complex distribution of fluid pressure on bedding interface cannot be obtained. Nevertheless, our numerical experiment gives universal rules based on the fundamental scenarios, which is beneficial to reveal the mechanism of the influence of bedding interfaces.

The result of our numerical simulation shows only two types of interaction between hydraulic fracture and bedding interface, i.e., (i) hydraulic fractures cross over bedding interfaces, and (ii) hydraulic fracture terminates at bedding interface. This is because we use the same strength of rock and in-situ stress on both sides of the bedding interface. The maximum concentration of stress occurs at the point where hydraulic fracture meets the inner interface, so the hydraulic fracture continues to cross the outer bedding at the same point. The current model is difficult to explain the occurrence of stepped fractures in laboratory experiments (Tan et al., 2017). The stepped fracture occurs when hydraulic fracture crosses over the outer interface at a distance away from the intersection between hydraulic fracture and the inner bedding interface. This may have appeared due to the anisotropy of bedding interface permeability that was not considered in our model. Another possibility may lie in the weak point in the strength of rock along bedding interface. When the local stress is greater than the strength of rock at the weak point, the hydraulic fracture crosses over the outer interface preferably at the weak point.

The last point is that the KGD model (i.e., the plane strain two-

dimensional model) is suitable for explaining the hydraulic fracture propagation phenomenon when the height of fracture is larger than the length. The two-dimensional model in this paper does not consider the influence of bedding interfaces on fracture length. In the three-dimensional model, the slip of bedding interface leads to a competitive relationship among the width, height, and length of fracture, which is more complicated than the two-dimensional model. Nevertheless, the slip scenarios of bedding interface proposed in our paper are applicable in three-dimensional cases. It is valuable to classify different slip scenarios of bedding interface when we study the crossing process of hydraulic fracture through bedding interface.

## 5. Conclusions

In this paper, we have used the combined finite-discrete element method (FDEM) to investigate the characteristics and mechanisms of the propagation of hydraulic fractures considering the influence of slip and permeability of bedding interfaces. We have analyzed the relation of the parameters between the Rankine crack model in FDEM and the fracture model in linear elastic fracture mechanics. Furthermore, we have validated the numerical results of hydraulic fracturing in the toughness domain with the analytical solution of the KGD model. The results show that the FDEM model can appropriately simulate the process of hydraulic fracture propagation in the toughness domain. We set up three bedding interface slip scenarios based on the Coulomb's law of friction and compare the propagation of hydraulic fractures with different bedding interface permeabilities.

Our results show that when the strength of rock and in-situ stress on both sides of the bedding interface are the same, the slip of bedding interface determines whether the hydraulic fracture can cross over the bedding interface. If the bedding interface slips, the slip displacement relieves the stress concentrated at the tip of hydraulic fracture, and the hydraulic fracture is unable to cross over the bedding interface. The permeability of bedding interface only prolongs the time for hydraulic fractures to cross through the bedding interface, but does not prevent the crossing behavior. Bedding interface has a relatively simple effect on the crossing mode and the morphology of the resulting hydraulic fractures, while they could cause huge changes of fluid pressure and local stress along the bedding interface. Therefore, a more serious fracture interference phenomenon occurs when multi-cluster fracturing is performed in reservoirs with bedding interfaces. How to control the propagation of multi-cluster fractures to alleviate the interference under different slip scenarios and different bedding interface permeabilities, and how to determine a reasonable stage spacing and cluster spacing for the fracturing of the reservoir with abundant bedding interfaces are important problems for future work.

*CRediT authorship contribution statement*

**Shan Wu:** Conceptualization, Methodology, Formal analysis, Investigation, Data curation, Writing – original draft, Visualization. **Ke Gao:** Methodology, Formal analysis, Visualization, Writing – review & editing. **Yu Feng:** Validation, Investigation, Writing – review & editing. **Xiaolin Huang:** Investigation, Writing – review & editing.

## Declaration of Competing Interest

The authors declare that they have no known competing financial interests or personal relationships that could have appeared to influence the work reported in this paper.

## Acknowledgment

This work is financially supported by the subprojects of the Strategic Cooperation Technology Projects of CNPC and CUPB (ZLZX2020-01-08 and ZLZX2020-01-07), and the Natural Science Foundation of China (No. 51774236).

## References

Abbas, A.K., Flori, R.E., Alsaba, M., 2018. Laboratory Geomechanical Characterization of the Zubair Shale Formation. American Rock Mechanics Association, Seattle, Washington, p. 7.

Cai, C., Kang, Y., Yang, Y., Wang, X., Li, Y., Huang, M., Wu, J., 2020. The effect of shale bedding on supercritical $CO_2$ jet fracturing: A experimental study. J. Pet. Sci. Eng. 195, 107798.

Celleri, H.M., Sánchez, M., 2021. Hydraulic fracture propagation barriers induced by weak interfaces in anisotropic rocks. Int. J. Numer. Anal. Methods Geomech. 45, 2155–2173.

Chen, Z., Bunger, A., Zhang, X., Jeffrey, R.G., 2009. Cohesive zone finite element-based modeling of hydraulic fractures. Acta Mech. Solida Sin. 22, 443–452.

Ciezobka J, Courtier J and Wicker J (2018) Hydraulic fracturing test site (HFTS) – Project overview and summary of results. In; SPE/AAPG/SEG Unconventional Resources Technology Conference Houston,Texas,USA, 1-9.

Dontsov, E., 2017. An approximate solution for a plane strain hydraulic fracture that accounts for fracture toughness, fluid viscosity, and leak-off. Int. J. Fract. 205, 221–237.

Dontsov, E.V., Peirce, A.P., 2015. An enhanced pseudo-3D model for hydraulic fracturing accounting for viscous height growth, non-local elasticity, and lateral toughness. Eng. Fract. Mech. 142, 116–139.

Duan, K., Kwok, C.Y., Zhang, Q., Shang, J., 2020. On the initiation, propagation and reorientation of simultaneously-induced multiple hydraulic fractures. Comput. Geotech. 117.

Evans, R.H., Marathe, M.S., 1968. Microcracking and stress-strain curves for concrete in tension. Material Structure 1, 61–64.

Fu, P., Johnson, S.M., Carrigan, C.R., 2011. Simulating complex fracture systems in geothermal reservoirs using an explicitly coupled hydro-geomechanical model. 45th US Rock Mechanics/Geomechanics Symposium. OnePetro.

Gandossi, L., 2013. An overview of hydraulic fracturing and other formation stimulation technologies for shale gas production. 1-64.

Hudson, M.R., 2017. Numerical Simulation of Hydraulic Fracturing in Tight Gas Shale Reservoirs. University of Leeds.

Ju, Y., Wang, Y., Xu, B., Chen, J., Yang, Y., 2019. Numerical analysis of the effects of bedded interfaces on hydraulic fracture propagation in tight multilayered reservoirs considering hydro-mechanical coupling. J. Pet. Sci. Eng. 178, 356–375.

Ju, Y., Wu, G., Wang, Y., Liu, P., Yang, Y., 2021. 3D numerical model for hydraulic fracture propagation in tight ductile reservoirs, considering multiple influencing factors via the entropy weight method. SPE J. 1–18.

Khristianovic, S.A., Zheltov, Y.P., 1955. Formation of vertical fractures by means of highly viscous liquid. 4th World Petrol. Cong. OnePetro 579–586.

Knight, E.E., Rougier, E., Lei, Z., Euser, B., Chau, V., Boyce, S.H., Gao, K., Okubo, K., Froment, M., 2020. HOSS: an implementation of the combined finite-discrete element method. Computational Particle Mech. 7, 765–787.

Lecampion, B., Bunger, A., Zhang, X., 2018. Numerical methods for hydraulic fracture propagation: a review of recent trends. J. Nat. Gas Sci. Eng. 49, 66–83.

Lei, Q., Gholizadeh Doonechaly, N., Tsang, C.-F., 2021. Modelling fluid injection-induced fracture activation, damage growth, seismicity occurrence and connectivity change in naturally fractured rocks. Int. J. Rock Mech. Min. Sci. 138, 104598.

Li, N., Zhang, S., Zou, Y., Ma, X., Wu, S., Zhang, Y., 2018a. Experimental analysis of hydraulic fracture growth and acoustic emission response in a layered formation. Rock Mech. Rock Eng. 51, 1047–1062.

Li, N., Zhang, S., Zou, Y., Ma, X., Zhang, Z., Li, S., Chen, M., Sun, Y., 2018b. Acoustic emission response of laboratory hydraulic fracturing in layered shale. Rock Mech. Rock Eng. 51, 3395–3406.

Ling, B., Khan, H.J., Druhan, J.L., Battiato, I., 2021. Multi-Scale microfluidics for transport in shale fabric. Energies 14, 21.

Lisjak, A., Kaifosh, P., He, L., Tatone, B., Mahabadi, O., Grasselli, G., 2017. A 2D, fully-coupled, hydro-mechanical, FDEM formulation for modelling fracturing processes in discontinuous, porous rock masses. Comput. Geotech. 81, 1–18.

Lisjak, A., Liu, Q., Zhao, Q., Mahabadi, O.K., Grasselli, G., 2013. Numerical simulation of acoustic emission in brittle rocks by two-dimensional finite-discrete element analysis. Geophys. J. Int. 195, 423–443.

Liu, N., Zhang, Z., Zou, Y., Ma, X., Zhang, Y., 2018. Propagation law of hydraulic fractures during multi-staged horizontal well fracturing in a tight reservoir. Pet. Explor. Dev. 45, 1129–1138.

Liu, X., Rasouli, V., Guo, T., Qu, Z., Sun, Y., Damjanac, B., 2020. Numerical simulation of stress shadow in multiple cluster hydraulic fracturing in horizontal wells based on lattice modelling. Eng. Fract. Mech. 238, 107278.

Mahabadi, O., Lisjak, A., He, L., Tatone, B., Kaifosh, P., Grasselli, G., 2016. Development of a new fully-parallel finite-discrete element code: Irazu, 50th US. Rock Mechanics/Geomechanics Symposium, OnePetro.

Mohammadnejad, M., Liu, H., Chan, A., Dehkhoda, S., Fukuda, D., 2021. An overview on advances in computational fracture mechanics of rock. Geosyst. Eng. 24, 206–229.

Munjiza, A., Andrews, K., 2000. Penalty function method for combined finite–discrete element systems comprising large number of separate bodies. Int. J. Numer. Methods Eng. 49, 1377–1396.

Munjiza, A., Smoljanović, H., Živaljić, N., Mihanovic, A., Divić, V., Uzelac, I., Nikolić, Ž., Balić, I., Trogrlić, B., 2020. Structural applications of the combined finite–discrete element method. Computational Particle Mechanics 7, 1029–1046.

Munjiza, A.A., 1992. Discrete elements in transient dynamics of fractured media. Swansea University. PhD Thesis.

Nagel, N., Zhang, F., Sanchez-Nagel, M., Lee, B., Agharazi, A., 2013. Stress shadow evaluations for completion design in unconventional plays. In: SPE Unconventional Resources Conference Canada. Calgary, Alberta, Canada,.

Profit, M., Dutko, M., Yu, J., Armstrong, J., Parfitt, D., Mutlu, U., 2016a. Application of state of the art hydraulic fracture modelling techniques for safe-optimized design and for enhanced production. 50th US Rock Mechanics/Geomechanics Symposium. OnePetro.

Profit, M., Dutko, M., Yu, J., Cole, S., Angus, D., Baird, A., 2016b. Complementary hydro-mechanical coupled finite/discrete element and microseismic modelling to predict hydraulic fracture propagation in tight shale reservoirs. Computational Particle Mech. 3, 229–248.

Rockfield, S.L., 2016. ELFEN User Manual. Rockfield Software Ltd., Swansea.

Smoljanović, H., Živaljić, N., Nikolić, Ž., Munjiza, A., 2018. Numerical analysis of 3D dry-stone masonry structures by combined finite-discrete element method. Int. J. Solids Struct. 136, 150–167.

Taghichian, A., Zaman, M., Devegowda, D., 2014. Stress shadow size and aperture of hydraulic fractures in unconventional shales. J. Pet. Sci. Eng. 124, 209–221.

Tan, P., Jin, Y., Han, K., Hou, B., Chen, M., Guo, X., Gao, J., 2017. Analysis of hydraulic fracture initiation and vertical propagation behavior in laminated shale formation. Fuel 206, 482–493.

Tan, P., Jin, Y., Pang, H., 2021. Hydraulic fracture vertical propagation behavior in transversely isotropic layered shale formation with transition zone using XFEM-based CZM method. Eng. Fract. Mech. 248, 107707.

Tang, J., Wu, K., 2018. A 3-D model for simulation of weak interface slippage for fracture height containment in shale reservoirs. Int. J. Solids Struct. 144–145, 248–264.

Tang, J., Wu, K., Zeng, B., Huang, H., Hu, X., Guo, X., Zuo, L., 2018. Investigate effects of weak bedding interfaces on fracture geometry in unconventional reservoirs. J. Pet. Sci. Eng. 165, 992–1009.

Vega, B., Ross, C.M., Kovscek, A.R., 2015. Imaging-Based Characterization of Calcite-Filled Fractures and Porosity in Shales. SPE J. 20, 810–823.

Wang, M., Gao, K., Feng, Y.T., 2021a. An improved continuum-based finite–discrete element method with intra-element fracturing algorithm. Comput. Methods Appl. Mech. Eng. 384, 113978.

Wang, Q., Gale, J.F., 2016. Characterizing bedding-parallel fractures in shale: aperture-size distributions and spatial organization. AAPG Annual Convention and Exhibition.

Wang, Y., Ju, Y., Zhang, H., Gong, S., Song, J., Li, Y., Chen, J., 2021b. Adaptive finite element-discrete element analysis for the stress shadow effects and fracture interaction behaviours in three-dimensional multistage hydrofracturing considering varying perforation cluster spaces and fracturing scenarios of horizontal wells. Rock Mech. Rock Eng. 54, 1815–1839.

Wu, M., Gao, K., Song, Z., Liu, J., 2021. Effects of Rock Heterogeneity on Hydraulic Fracture Propagation: A Numerical Study Based on the Combined Finite-Discrete Element Method. 55th US Rock Mechanics/Geomechanics Symposium. OnePetro.

Wu, S., Li, T., Ge, H., Wang, X., Li, N., Zou, Y., 2019. Shear-tensile fractures in hydraulic fracturing network of layered shale. J. Pet. Sci. Eng. 183.

Xu, W., Prioul, R., Berard, T., Weng, X., Kresse, O., 2019. Barriers to hydraulic fracture height growth: A new model for sliding interfaces. SPE Hydraulic Fracturing Technology Conference and Exhibition. OnePetro.

Yan, C., Jiao, Y.Y., Zheng, H., 2018. A fully coupled three-dimensional hydro-mechanical finite discrete element approach with real porous seepage for simulating 3D hydraulic fracturing. Comput. Geotech. 96, 73–89.

Yan, C., Zheng, H., Sun, G., Ge, X., 2016. Combined finite-discrete element method for simulation of hydraulic fracturing. Rock Mech. Rock Eng. 49, 1389–1410.

Yang, Y., Ren, X., Zhou, L., Lu, Y., 2020. Numerical study on competitive propagation of multi-perforation fractures considering full hydro-mechanical coupling in fracture-pore dual systems. J. Pet. Sci. Eng. 191, 107109.

Zhang, F., Dontsov, E., 2018. Modeling hydraulic fracture propagation and proppant transport in a two-layer formation with stress drop. Eng. Fract. Mech. 199, 705–720.

Zhang, S., Li, S., Zou, Y., Li, J., Ma, X., Zhang, X., Zhang, Z., Wu, S., 2021a. Experimental study on fracture height propagation during multi-stage fracturing of horizontal wells in shale oil reservoir. J. China Univ. Petroleum (Ed. Nat. Sci.) 45, 77–86.

Zhang, Z., Zhang, S., Zou, Y., Ma, X., Li, N., Liu, L., 2021b. Experimental investigation into simultaneous and sequential propagation of multiple closely spaced fractures in a horizontal well. J. Pet. Sci. Eng. 202, 108531.

Zhao, Q., Lisjak, A., Mahabadi, O., Liu, Q., Grasselli, G., 2014. Numerical simulation of hydraulic fracturing and associated microseismicity using finite-discrete element method. J. Rock Mech. Geotech. Eng. 6, 574–581.

Zou, Y., Ma, X., Zhou, T., Li, N., Chen, M., Li, S., Zhang, Y., Li, H., 2017. Hydraulic Fracture Growth in a Layered Formation based on Fracturing Experiments and Discrete Element Modeling. Rock Mech. Rock Eng. 50, 2381–2395.

Zou, Y., Zhang, S., Zhou, T., Zhou, X., Guo, T., 2016. Experimental investigation into hydraulic fracture network propagation in gas shales using CT scanning technology. Rock Mech. Rock Eng. 49, 33–45.